

Deep ATLAS Radio Observations of the ELAIS-S1/*Spitzer* Wide-Area Infrared Extragalactic field

Enno Middelberg

*Astronomisches Institut der Universität Bochum, Universitätsstr. 150, 44801 Bochum,
Germany; middelberg@astro.rub.de*

Ray P. Norris

Australia Telescope National Facility, PO Box 76, Epping NSW 1710, Australia

Tim J. Cornwell

Australia Telescope National Facility, PO Box 76, Epping NSW 1710, Australia

Maxim A. Voronkov

Australia Telescope National Facility, PO Box 76, Epping NSW 1710, Australia

Brian D. Siana

Spitzer Science Center, California Institute of Technology, MS 220-6, Pasadena, CA 91125

Brian J. Boyle

Australia Telescope National Facility, PO Box 76, Epping NSW 1710, Australia

Paolo Ciliegi

INAF, Osservatorio Astronomico di Bologna, Via Ranzani 1, I-40127 Bologna, Italy

Carole A. Jackson

Australia Telescope National Facility, PO Box 76, Epping NSW 1710, Australia

Minh T. Huynh

Spitzer Science Center, California Institute of Technology, MS 220-6, Pasadena, CA 91125

Stefano Berta

*Dipartimento di Astronomia, Università di Padova, Vicolo dell'Osservatorio 2, 35122
Padova, Italy*

Stefano Rubele

*Dipartimento di Astronomia, Università di Padova, Vicolo dell'Osservatorio 2, 35122
Padova, Italy*

Carol J. Lonsdale

*Center for Astrophysics and Space Sciences, University of California at San Diego, 9500
Gilman Drive, La Jolla, CA 92093-0424*

Rob J. Ivison

UK Astronomy Technology Centre, Royal Observatory, Blackford Hill, Edinburgh EH9 3HJ

Ian Smail

*Institute for Computational Cosmology, Durham University, South Road, Durham DH1
3LE, UK*

Seb J. Oliver

Astronomy Centre, CPES, University of Sussex, Falmer, Brighton BN1 9QJ, UK

ABSTRACT

We have conducted sensitive ($1\sigma < 30\ \mu\text{Jy}$) 1.4 GHz radio observations with the Australia Telescope Compact Array of a field largely coincident with infrared observations of the *Spitzer* Wide-Area Extragalactic Survey. The field is centred on the European Large Area ISO Survey S1 region and has a total area of 3.9° . We describe the observations and calibration, source extraction, and cross-matching to infrared sources. Two catalogues are presented; one of the radio components found in the image and one of radio sources with counterparts in the infrared and extracted from the literature. 1366 radio components were grouped into 1276 sources, 1183 of which were matched to infrared sources. We discover 31 radio sources with no infrared counterpart at all, adding to the class of Infrared-Faint Radio Sources.

Subject headings: Catalogs, Galaxies: Active, Galaxies: Evolution, Radio Continuum: Galaxies, Surveys

1. Introduction

In this paper describing early results from the Australia Telescope Large Area Survey (ATLAS), we present a 1.4 GHz survey of the European Large Area ISO Survey (ELAIS) S1 field (Oliver et al. 2000). This is the second survey paper describing results from ATLAS, and is complementary to the paper by Norris et al. (2006), which describes observations of the Chandra Deep Field South.

ATLAS is an ambitious study of galaxies and their evolution since $z \gtrsim 3$, using predominantly observations in the radio regime. Two large areas (about 3.5 deg^2 each) have been surveyed with high sensitivity, using the Australia Telescope Compact Array (ATCA) at 1.4 GHz, to complement multi-wavelength observations in the infrared with the *Spitzer* Space Telescope. The immediate goals of the observations are, in brief, to determine whether the radio-infrared relation holds at high redshifts; to search for overdensities of high- z ULIRGs which mark the positions of protoclusters in the early universe; to trace the radio luminosity function to high redshifts; to determine the relative contribution of starbursts and AGN to the overall energy density of the universe; and to open a new parameter space to allow for serendipitous discovery of rare sources. However, surveys such as this have proven in the past to have a substantial impact on longer time-scales, when they are used as a resource in a broad variety of studies.

It was decided early on in this project to observe two separate sky regions, rather than one larger area, to exclude cosmic variance which might affect the results. Both fields extend beyond 2° in one dimension, which is sufficient to sample structures at any one redshift which have evolved to more than 150 Mpc at the present epoch. Nevertheless, such surveys are still prone to cosmic variance. The CDFS is known to contain some large-scale structures (Vanzella et al. 2005 and references therein), predominantly at redshifts of 0.73 and 1.1. These structures are not obvious clusters, but “sheets” in the original CDFS. This finding demonstrates the need to sample large areas for an unbiased view of galaxy formation.

It should be noted that the ELAIS-S1 field has been also observed by Gruppioni et al. (1999) using the ATCA in June 1997, reaching a fairly uniform rms of $80 \mu\text{Jy}$ across the observed area, a factor of three higher than the average rms in our current observations. Also, the area they observed is slightly larger than the field described here. We have cross-matched their sources to ours and briefly discuss the results.

This paper is organised as follows. Section 2 describes the observations and Section 3 details the source extraction process and the cross-identification of radio sources with the SWIRE catalogue. Section 4 provides a description of the catalogues and the literature search for counterparts in other surveys. Section 5 gives a description of the classification

and a few individual sources are described in more detail in Section 6. We provide a short analysis of the radio-infrared relation in Section 7 and our conclusions in Section 8.

2. Observations

As of December 2006 we have completed about 50% of the planned observations of the ELAIS-S1 field. The sensitivity here is slightly higher than in the CDFS, partly because of slightly longer integration times (between 10.5 h per pointing and 13.5 h per pointing, compared to 8.2 h per pointing over most of the CDFS), and partly because there is a strong interfering source in the CDFS field. However, a 3.8 Jy source (PKS 0033-44) limits the dynamic range of the ELAIS-S1 observations even though it is well outside our pointings. An overview of the observed area is reproduced in Figure 1.

2.1. Radio observations

The radio observations were carried out on 27 separate days between 9 January 2004 and 24 June 2005 with the Australia Telescope Compact Array (ATCA), with a total net integration time on the pointings of 231 h, in a variety of configurations to maximise the (u, v) coverage (Table 1). However, (u, v) coverage is probably not a crucial factor in aperture synthesis when the field is dominated by point sources as in our case. 3.89 deg^2 in the ELAIS-S1 field were analysed (this is the total area in the mosaic where the primary beam response is $> 10\%$) in a mosaic consisting of 20 overlapping pointings (Table 2). The full width at half maximum (FWHM) of the primary beams at 1.4 GHz is $35'$. The pointings were observed for one minute each, and the calibrator 0022-423 was observed after each cycle of 20 pointings for two minutes. Amplitude calibration was done using PKS 1934-638 as a primary calibrator, which was observed for 10 min before or after each observing run. It was assumed to have a flux density of 15.012 Jy at 1.34 GHz and 14.838 Jy at 1.43 GHz, corresponding to the centres of the two ATCA frequency bands. Each band had a bandwidth of 128 MHz over 33 channels, so the total observing bandwidth was 256 MHz. In the observation in early 2004, the higher band was only slightly affected by terrestrial radio-frequency interference (RFI), but this deteriorated in 2004, requiring considerable effort to edit the data properly to avoid losing a large fraction of good data. The lower band was mostly free of RFI and required little editing. In the early stages of the project in 2004, only pointings 1-12 were observed (the upper three rows of circles in Figure 1), but the surveyed area was extended in 2005 by adding pointings 13-20 to the field. The new pointings were initially observed for a longer time to catch up with the older pointings, resulting in a different (u, v) coverage

and a little more integration time. Pointings 1-12 have net integration times of 10.5 h per pointing, whereas pointings 13-20 have net integration times of 13.5 h per pointing. After editing, the predicted noise level is $22 \mu\text{Jy}$ in the centre of the mosaic. Towards the image edges, the noise level increases due to primary beam attenuation.

2.1.1. Calibration

The data were calibrated using Miriad (Sault et al. 1995) standard procedures, following recommendations for high dynamic range imaging. The raw data come in RPFITS format, and are converted into the native Miriad format using ATLOD. ATLOD discarded every other frequency channel (which are not independent from one another, hence no information is lost) and flagged one channel in the higher-frequency band which contained a multiple of 128 MHz, and thus was affected by self-interference at the ATCA. We also did not use the channels at either end of the band where the sensitivity dropped significantly. The resulting data set contained two frequency bands, with 13 channels and 12 channels respectively, all of which are 8 MHz wide, and so the total net bandwidth in the data was $25 \times 8 \text{ MHz} = 200 \text{ MHz}$.

The data were bandpass-calibrated to prepare for RFI removal with Pieflag (Middelberg 2006). Pieflag derives baseline-based statistics from a channel which is free of, or only very slightly affected by, RFI, and searches the other channels for outliers and sections of high noise. It is therefore important to bandpass-calibrate the data before using it. Pieflag eliminated all RFI-affected data which would have been flagged in a visual inspection, while minimising the amount of erroneously flagged good data. On average, approximately 3% and 15% of the data were flagged in the lower and higher band, respectively.

After flagging, the bandpass calibration was removed as it may have been affected by RFI in the calibrator observations, and repeated. Phase and amplitude fluctuations throughout each observing run were corrected using the interleaved calibrator scans, and the amplitudes were scaled by correction factors derived from the observations of the primary calibrator. The data were then split by pointing and imaged.

2.1.2. Imaging

The data for each of the 20 pointings were imaged separately using uniform weighting and a pixel size of $2.0''$. The 25 frequency channels were gridded separately to increase the (u, v) coverage. The relatively high fractional bandwidth of the observations (15%) required the use of Miriad's implementation of multi-frequency clean, MFCLEAN, for deconvolution,

to account for spectral indices across the observed bandwidth and to reduce sidelobes. After a first iteration, model components with a flux density of more than 1 mJy beam^{-1} were used in phase self-calibration, to correct residual phase errors. The data were then re-imaged and cleaned with 5000 iterations, at which point the sidelobes of strong sources were found to be well below the thermal noise. The models were convolved with a Gaussian of $10.26'' \times 7.17''$ diameter at position angle 0° , and the residuals were added. The restored images of the 20 pointings were merged in a linear mosaic using the Miriad task LINMOS, which divides each image by a model of the primary beam to account for the attenuation towards the edges of the image, and then uses a weighted average for pixels which are covered by more than one pointing. As a result, pixels at the mosaic edges have a higher noise level. Regions beyond a perimeter where the primary beam response drops below 3% (this occurs at a radius of $35.06'$ from the centre of a pointing) were blanked.

Imaging of the data turned out to be challenging, but the sensitivity of the image presented here is mostly within 25% of the predicted sensitivity. In the south-eastern corner of the mosaic, mild artefacts remain due to the presence of the 3.8 Jy radio source PKS 0033-44, which is located about 1° away from the centre of pointing 13. The noise level of the present image could only be reached by including this source in the CLEANed area. Because of a combination of the high resolution of the image, the distance of the source from the pointing centre, and the requirement of multi-frequency clean to provide images which are three times larger than the area to clean, we had to generate very large images with 16384 pixels on a side, plus an additional layer of the same extent for the spectral index. These images cannot be handled by 32-bit computers because the required memory exceeds their address space, and we had to employ a 64-bit machine to image the data.

The cause of the residual sidelobes is still the subject of investigation. At present, we suspect that non-circularities in the sidelobe pattern of the primary beams are the culprit. The interfering source sits on the maximum of the first antenna sidelobe and, in the course of the observations, rotates through the sidelobe pattern due to the azimuthal mounting of the antennas. We have measured the primary beam response of two ATCA antennas in great detail using a geostationary satellite at 1.557 GHz, and derived a model of their far-field reception patterns. Unfortunately, we were unable to reproduce the sidelobe pattern arising from PKS 0033-44, and no correction from this exercise has been applied to our data.

2.1.3. *Image properties*

The sensitivity is not uniform across the image due to primary beam attenuation, however, it is quite homogeneous in the central 1 deg^2 of the image. A cumulative histogram of

an image of the noise in this area, made with SExtractor (Bertin & Arnouts 1996), revealed that only 2% of the image has a noise of $22\ \mu\text{Jy}$ or less, consistent with the theoretical expectations. However, 75% of pixels have a noise of $27.5\ \mu\text{Jy}$ or less, which is 25% higher than the expected noise. We conclude that in the regions which are not affected by sidelobes from PKS 0033-44 the sensitivity of the image is close to the theoretical expectations.

2.1.4. *Clean bias*

Clean bias is an effect in deconvolution which redistributes flux from point sources to noise peaks in the image, thereby reducing the flux density of the real sources. As the amount of flux which is taken away from real sources is independent of the sources' flux densities, the fractional error this causes is largest for weak sources. The effect of clean bias in our calibration procedure has been analysed as follows. We have added to the data of one pointing (rms= $30\ \mu\text{Jy}$) 132 point sources at random positions, with flux densities between $150\ \mu\text{Jy}$ and $3\ \text{mJy}$. The number of sources added with a particular SNR were N=40 ($5\ \sigma$), 15 ($6\ \sigma$), 15 ($7\ \sigma$), 15 ($8\ \sigma$), 15 ($9\ \sigma$), 10 ($10\ \sigma$), 10 ($12\ \sigma$), 5 ($16\ \sigma$), 3 ($20\ \sigma$), 2 ($30\ \sigma$), 1 ($50\ \sigma$), and 1 ($100\ \sigma$).

The data have then been used to form an image in the same way as the final image was made, and each source's flux density was extracted using a Gaussian fit, and then divided by the injected flux density. This test was repeated 30 times to build up significant statistics, in particular for the sources with high SNR. We found that using 5000 iterations in cleaning did not cause a significant clean bias ($< 2.5\%$), whereas using 50000 iterations did cause the extracted fluxes to be reduced by up to 5% (Figure 3). We conclude that the flux densities in our catalogue are only marginally affected by clean bias.

2.1.5. *Comparison to earlier observations*

We have compared the flux densities and positions of components in our image to those of Gruppioni et al. (1999) (G99). We have obtained their image and selected 83 isolated components with $S > 0.5\ \text{mJy}$ in regions where our noise level was below $30\ \mu\text{Jy}$. All sources were detected with an SNR >6 by G99. These sources were grouped into bins with $2^n\ \text{mJy}$ to $2^{n+1}\ \text{mJy}$ (n=-1,0,1,2,3,4), the flux densities were extracted from G99's image using the same methods as for our image, and the ratios S/S_{G99} were computed. The median ratios were 1.36 (0.5 mJy-1 mJy), 1.43 (1 mJy-2 mJy), 1.19 (2 mJy-4 mJy), and 1.16 (4 mJy-8 mJy). The two highest bins with 8 mJy-16 mJy and 16 mJy-32 mJy had ratios very close to one,

but only two measurements each, hence the statistics are not reliable.

Our analysis suggests that our flux densities are systematically higher than G99’s, although S/S_{G99} appears to approach unity towards higher flux densities. We have found that our flux extraction procedure reproduces the catalogued fluxes of G99 to within 3%, hence we conclude that our procedure is working and the effect is real. The cause of this discrepancy is not known, but possible explanations are (i) calibration differences: G99 used amplitude self-calibration with a relatively sparse array and very short solution intervals, which may have affected the flux densities. We did not use amplitude self-calibration at all because it was not found to improve our image significantly; (ii) (u, v) coverage: G99 had only one configuration at the ATCA whereas we had six, yielding more constraints in deconvolution. Also G99 imaged the data from both IF bands separately and averaged the images later, thus using only one half of their data in the deconvolution stage.

We also tested for a systematic position offset between the components of G99 and ours. We found a mean offset of $0.112'' \pm 0.016''$ in right ascension and of $0.017'' \pm 0.022''$ in declination, and conclude that systematic position offsets are negligible.

2.2. *Spitzer* observations

The *Spitzer* observations of the ELAIS-S1 field were carried out as part of the *Spitzer* Wide-Area Infra-Red Extragalactic Survey (SWIRE) program, as described by Lonsdale et al. (2003). Approximately 6.9 deg^2 were observed in the ELAIS-S1 region at $3.6 \mu\text{m}$, $4.5 \mu\text{m}$, $5.8 \mu\text{m}$, and $8.0 \mu\text{m}$ with the Infrared Array Camera (IRAC) and at $24 \mu\text{m}$ with the Multi-band Imaging Photometer (MIPS). The sensitivities in the five bands are $4.1 \mu\text{Jy}$, $8.5 \mu\text{Jy}$, $48.2 \mu\text{Jy}$, $53.0 \mu\text{Jy}$, and $252 \mu\text{Jy}$. Here we use the fourth data release, containing more than 400.000 sources (Surace et al. 2007, in prep.).

2.3. Optical observations

The optical follow-up observations of the ELAIS-S1 field are called the ESO-*Spitzer* Imaging Extragalactic Survey (ESIS). The observations were carried out with the Wide Field Imager (WFI) of the 2.2 m La Silla ESO-MPI telescope and with the VISIBLE Multi Object Spectrograph (VIMOS) on the VLT, to cover 5 deg^2 in BVRIZ. Only approximately 1.5 deg^2 have yet been covered (Berta et al. 2006) with WFI and these data are included in our catalogue. The filters used are WFI B/99 (later replaced by B/123), V/89 and Rc/162, and the catalogue is 95% complete at 25^{m} in the B and V bands, and at 24.5^{m} in the R

band (all in Vega units).

3. Image analysis

3.1. Component extraction

This section describes the procedure we used to extract radio sources from the image and to subsequently match these radio sources to infrared sources. In our terminology, a radio component is a region of radio emission which is best described by a Gaussian. Close radio doubles are very likely to be best represented by two Gaussians and are therefore deemed to consist of two components. Single or multiple components are called a radio source if they are deemed to belong to the same object.

The rms of the image varies from $22 \mu\text{Jy}$ in the best regions to 1 mJy towards the edges of the image, caused by primary beam attenuation. It is therefore not possible to use the same cutoff, in terms of flux density per pixel, above which a pixel is deemed a detection of a source and below which pixels are deemed noise. Furthermore, flux densities measured towards the image edges are increasingly affected by uncertainties in the primary beam model, and we therefore restricted our image analysis to those sources which lie in regions where the theoretical sensitivity is below $250 \mu\text{Jy}$.

We used SExtractor to create an image of the noise, by which we divided the radio image to obtain an image of signal-to-noise (called the SNR map). The SNR map has unity noise everywhere, and can be analysed using a single criterion. We used the Miriad task IMSAD to look for islands of $\text{SNR} > 5$, and then used this catalogue as input for a visual inspection of the total intensity image at the locations where $\text{SNR} > 5$. Sources were re-fitted using the total intensity image, and were subsequently cross-identified with IR sources and classified. If either of the two axes of a fitted Gaussian was smaller than the restoring beam's corresponding axis, the fit was repeated using a Gaussian with the major and minor axis fixed to the restoring beam and the position angle set to zero. Also very weak sources were in general found to be better represented with fixed-size Gaussians.

The integrated flux densities of extended sources were obtained by integrating over the source area, rather than summing the flux densities of their constituents. This is because even multiple Gaussians are seldom a proper representation of extended sources, and, using this technique, even very faint emission between components is included.

We estimated the error of the integrated flux densities using Eq. (1) in Schinnerer et al. (2004), which is based on Condon (1997), assuming a relative error of the flux calibration of

5% whereas Schinnerer et al. (2004) assumed 1%. In the case of extended sources, where the integrated flux density was measured by integrating over a polygon in the image, we assumed a 5% scaling error and added to that in quadrature an empirical error arising from the shape and size of the area over which was integrated:

$$\Delta S = \sqrt{(0.05S)^2 + (10^{-7}/S)^2} \quad (1)$$

where S is the flux density in Jy. For extended sources with 10 mJy, 1 mJy and 0.5 mJy, the total errors are thus 0.5 mJy (5%), 0.11 mJy (11%), and 0.2 mJy (40%), respectively, which describe the errors found empirically reasonably well.

The uncertainties in the peak flux densities were estimated using Eq. (21) in Condon (1997). Errors in right ascension and declination are the formal errors from Gaussian fits plus a 0.1" uncertainty from the calibrator position added in quadrature.

3.1.1. Deconvolution of components from the restoring beam

All radio components were deconvolved from the restoring beam. If a deconvolution was not possible, or the deconvolution yielded a point source, the component was deemed to be unresolved and the deconvolved size has been left blank in Table 4.

3.2. The cross-identification process

The cross-matching process was as follows. The region used for the fit and the ellipse indicating the FWHM were inspected, along with the corresponding parts of the following images: the SNR map, a naturally weighted radio image with lower resolution (and slightly higher sensitivity), a superuniformly weighted radio image with higher resolution (but lower sensitivity), and the 3.6 μ m SWIRE image with superimposed SNR map contours. Furthermore, the locations of catalogued SWIRE sources within 30" of the fitted coordinates were shown on the SWIRE images.

It was then decided (i) whether each radio component was a genuine detection or likely to be a sidelobe, (ii) how it could be matched to catalogued or uncatalogued SWIRE sources, (iii) whether multiple radio components constituted radio emission from a single object, and (iv) whether extended components needed to be divided into sub-components. Emission deemed to be sidelobes was found predominantly towards the edges of the image and associated with, and directly adjacent to, strong sources.

Most sidelobes were discovered because the naturally-weighted image, which has a different sidelobe pattern and higher sensitivity but lower resolution, showed no evidence of a source at the position of a possible source in the uniformly weighted image. Our catalogue of radio components contains 1366 components; 15 were deemed to be sidelobes and have been marked as such (all with $\text{SNR} < 6$), leaving 1351 genuine radio components.

The separation between a radio component and a SWIRE source cannot easily be used as a parameter in the cross-identification process. In some cases, despite a relatively large separation, the cross-identification is relatively clear because the SWIRE source is extended towards the radio component, such as in the examples shown in Figure 4.

1134 radio components (88.9%) could be characterized properly by a single Gaussian and were judged to be the only radio counterpart of a catalogued SWIRE source. A fraction of these displayed the morphology of doubles in a superuniformly weighted image. 15 sources (1.2%) had uncatalogued SWIRE counterparts.

32 sources (2.5%) were deemed to be radio doubles, consisting of two radio components; and 26 sources (2.0%) consisted of two or more components, displaying more complex morphologies like triplets or core-jet morphologies.

We have tested for systematic radio-IR position offsets by calculating the average offsets of 533 sources which consist of a single radio component and a catalogued SWIRE counterpart, and have $\text{SNR} > 10$. The offsets have a mean of $(0.08 \pm 0.03)''$ in right ascension and $(0.06 \pm 0.03)''$ in declination. Although the offset is formally significantly different from zero, we note that it is less than a tenth of a pixel in the radio image.

All sources classified as radio doubles have been reviewed using the criteria developed by Magliocchetti et al. (1998) based on an analysis of the FIRST survey (Becker et al. 1995): Two radio components are likely to be part of a double when (a) their separation measured in arcsec is less than $100(S/100)^{0.5}$, where S is the total flux of the two constituents, and (b) their flux densities do not differ by more than a factor of four. We give the results of this test in the source table. It should be noted that the test has been derived from a large sample of galaxies (236000) and is purely empirical. Furthermore, the FIRST survey is shallower ($\text{rms} = 0.14 \text{ mJy}$) than ours, and so statistically may contain different objects from the survey presented here. It is therefore no surprise that some of our radio sources which are clearly radio doubles fail the test. For example, S923 (Figure 8) fails on criterion (a), but satisfies criterion (b).

3.3. The false cross-identification rate

Because the SWIRE field has a high IR source density (58700 sources per deg^2), there is some chance that a radio component falls within a few arcseconds of an infrared source, although it is not physically connected to it. The two sources would be wrongly cross-matched, and hence there is a fraction of erroneous cross-identifications in our source catalogue, an upper limit of which we estimate as follows.

From the source density, one can calculate that on average 0.01423 SWIRE sources fall within $1''$ of any one point in the field. The number of SWIRE sources within $1'' - 2''$ of any one point is 0.0427, and within $2'' - 3''$ is 0.0711. We have confirmed these numbers experimentally by searching near several hundred random positions in the SWIRE catalogue.

In our catalogue, 1134 sources consist of a single component and have a good SWIRE cross-identification. Of these, 656 have a separation of less than $1''$, 350 have a separation of $1'' - 2''$, 86 have a separation of $2'' - 3''$, and 45 have a separation of more than $3''$.

Of the original 1134 cross-identifications, a fraction of 0.01423, or 16 sources, are expected to be purely coincidental, and are found among the 656 sources with sub-arcsec cross-identifications. Thus, a fraction of $16/656 = 0.024$ is likely to be coincidental (and wrong).

With the sub-arcsec cross-identifications now accounted for, $(1134 - 656) = 478$ sources remain. Of these, a fraction of 0.0427, or 20 sources, will fall within $1'' - 2''$ of an infrared source by coincidence. Thus, a fraction of $20/481 = 0.042$ is coincidental.

Repeating the steps above leaves $(1134 - 656 - 350) = 128$ sources which have not yet been cross-identified. Putting 128 sources randomly on the SWIRE image yields a coincidental counterpart within $2'' - 3''$ for a fraction of 0.0711, or 9 sources. Thus, a fraction of $9/86 = 0.105$ is coincidental. The statistics of the remaining 45 sources with separations $> 3''$ are not meaningful because the separations are dominated by extended radio objects which are not expected to coincide with infrared sources. A summary of this estimate is shown in Table 3.

We stress that the rates of false cross-identifications given here are upper limits. A false cross-identification does not only require a false counterpart within a few arcseconds of the radio position, but it also requires that the true counterpart is much fainter than the false one. The second requirement reduces the rate of false cross-identifications well below our estimate.

4. The component and source catalogues

Following Norris et al. (2006) we publish two catalogues, one containing the component data (Table 4), and one containing radio sources and their infrared counterparts (Table 5).

4.1. The components catalogue

The component catalogue contains information about Gaussian components fitted to the radio image. It does not contain information about the grouping of components to sources, which is exclusively left to the source catalogue in the next section.

4.2. The source catalogue

The distribution of integrated flux densities for the 1276 catalogued sources is shown in Figure 5. We have carried out a Kolmogorov-Smirnov-test using the ELAIS-S1 and CDFS integrated flux densities, to test the likelihood that the two samples are drawn from the same parent distribution. Because the two fields have different sensitivities, the catalogues cannot be compared in full, but a flux cutoff has to be used. Furthermore, we restricted the test to sources within 48' of the field centres and required an rms of between $30\ \mu\text{Jy}$ to $40\ \mu\text{Jy}$, to exclude regions with elevated noise levels towards the image edges. We find that when only sources with flux densities of more than 0.5 mJy are compared (ELAIS-S1: 137 sources, CDFS: 130 sources), the probability that the two samples are drawn from the same parent distribution is 73.7%. When the minimum required flux density is lowered to 0.4 mJy (ELAIS-S1: 179 sources, CDFS: 151 sources) or 0.3 mJy (ELAIS-S1: 222 sources, CDFS: 186 sources), the probabilities are 18.3% and 25.8%, respectively. We conclude that in regions with similar sensitivities the distribution of radio sources in the ELAIS-S1 and CDFS fields is identical at a flux density level of more than 0.3 mJy.

In the source catalogue, comments on the cross-match and the radio morphology are recorded as follows. If no comment is given, we had no doubt about the identification; "uncatalogued counterpart" means that we had no doubt that the radio source is associated with a clearly visible IR source at either $3.6\ \mu\text{m}$ or $24\ \mu\text{m}$ which is not listed in the SWIRE catalogue (data release 4); "IFRS" means that a radio source could not be reasonably matched to any IR counterpart at all and did not appear to be associated with another radio source; "confused XID" means that the radio source is likely to be associated with the SWIRE source we give, but that other sources cannot be ruled out; "unclear XID" means that the identification was too ambiguous to make a reasonable choice. We also comment on the

radio morphology if the source is anything but a single Gaussian. In the case of multiple-component sources we give the component numbers which were deemed to be associated with the source, and we comment on extension or blending with other radio sources. The coordinates of sources are generally those of the radio observations, but in the case of sources with more than one component and with a clear IR counterpart, the SWIRE coordinates have been adopted as the source position. In the case of more than one component without a clear IR component the flux-weighted mean of the radio components has been used.

4.3. Identification of sources with other catalogues and literature data

The ELAIS-S1 region has already been surveyed with the ATCA at 1.4 GHz by Gruppioni et al. (1999) with a 1σ sensitivity of $80\ \mu\text{Jy}$, and we have cross-matched their catalogue to ours, resulting in 366 matches. We have also searched the NASA Extragalactic Database¹ for objects within $2''$ of the sources in our catalogue, and found matches to 105 sources, sometimes with multiple names. We mostly give the designations from the ELAIS $15\ \mu\text{m}$ catalogue (Oliver et al. 2000), the APMUKS catalogue (Maddox et al. 1990), and the 2MASS catalogue (Skrutskie et al. 2006). These cross-identifications have been included in Table 5.

We searched for available redshifts and found that 59 objects within $2''$ of our sources had catalogued redshifts, mostly from La Franca et al. (2004). A histogram of the redshifts is shown in Figure 6. Unlike in the CDFS, there is no indication of cosmic large-scale structure in this histogram. However, the number of redshifts is small and may not be sufficient to show inconspicuous large-scale structure.

We have cross-matched our source catalogue to sources from the Sydney University Molonglo Sky Survey (SUMSS, Bock et al. 1999), which is a survey of the southern sky at 843 MHz, using the Molonglo Observatory Synthesis Telescope (MOST). The sensitivity of SUMSS is of the order of $\sim 1\ \text{mJy beam}^{-1}$, so that the faintest sources have a flux density of the order of $\sim 5\ \text{mJy}$. Assuming a spectral index of $\alpha = -0.7$ ($S \propto \alpha$), typical for radio emission from AGN, this corresponds to $S_{1.4\text{GHz}} = 3.5\ \text{mJy}$, so only the brightest ATLAS sources will be present in SUMSS. We found 73 matches to sources catalogued in the 1 June 2006 data release² and give the results in Table 6. There were no SUMSS sources without 1.4 GHz counterpart in the ATCA image.

We have also searched for counterparts in the AT20G survey (Ricci et al. 2004), which

¹<http://nedwww.ipac.caltech.edu/index.html>

²<http://www.astrop.physics.usyd.edu.au/sumsscat/>

is a survey of the southern sky with the ATCA at 18 GHz, but found no match.

5. Classification

5.1. AGN

Here we discuss the classification of sources as AGN based on their morphology, their ratio of $24\ \mu\text{m}$ to radio flux, and using literature information.

Radio sources exhibiting a double-lobed, triple, or more complex structures, e.g. with jets, were generally classified as AGN. Examples for classification based on morphology are S829, S923, S926, S930.1, S1192 and S1189, all of which are described in more detail in Section 6.

From *Spitzer* $24\ \mu\text{m}$ and VLA 20 cm detections in the First Look Survey (Condon et al. 2003), Appleton et al. (2004) derive $q_{24} = \log(S_{24\mu\text{m}}/S_{20\text{cm}}) = 0.84$. Here, sources with $\log(S_{24\mu\text{m}}/S_{20\text{cm}}) < -0.16$, i.e. more than 10 times the radio flux density as predicted by the radio-infrared relation, were classified as AGN.

In total 75 sources were classified as AGN based on their radio morphology, 128 sources based on their radio excess compared to the radio-infrared relation at $24\ \mu\text{m}$, and 9 sources had been classified as AGN by La Franca et al. (2004), based on optical spectroscopy. 14 sources were classified as AGN using more than one criterion, and thus 198 sources were classified as AGN. We note that, with the exception of the three sources S606, S717, and S813, all sources which were classified as AGN based on their morphology *and* which had catalogued $24\ \mu\text{m}$ flux densities were also classified as AGN based on their departure from the radio-infrared relation as given by Appleton et al. (2004). We plot the 20 cm flux densities as a function of $24\ \mu\text{m}$ flux densities of all sources in Figure 7. AGN are plotted separately according to how they have been classified.

5.2. Infrared-Faint Radio Sources (IFRS)

We find 31 sources with no detectable infrared counterpart. These sources have been dubbed “Infrared-Faint Radio Sources”, or IFRS, by Norris et al. (2006), and may be more extreme cases of the “Optically Invisible Radio Sources” found by Higdon et al. (2005). As they are invisible in the optical and infrared, there is only very limited information available. A Kolmogorov-Smirnov test reveals a 80.1% probability that the distribution of flux densities of the IFRS is drawn from the same parent distribution as all flux densities,

though the IFRS sources tend to have lower radio flux densities than the entire sample. We have carried out VLBI observations of three IFRS in our sample (S427, $S_{1.4\text{GHz}} = 21.4$ mJy; S509, $S_{1.4\text{GHz}} = 22.2$ mJy; and S775, $S_{1.4\text{GHz}} = 3.6$ mJy) to determine whether they are AGN hosts and the contribution to the arcsec-scale flux density from an AGN, but the results are not yet available. However, Norris et al. (2007) have successfully detected an IFRS in the CDF-S field.

6. Notes on individual sources

We comment on a few examples to illustrate the cross-identification process. The sources discussed here are shown in Figure 8.

- *Sources S829 and S829.2* S829 is an example of a mildly extended object, which is best represented with two Gaussians (C829 and C829.1). However, at higher resolution it begins to resemble a double-lobed or core-jet morphology, and it is centred on the IR source SWIRE4_J003251.97-433037.2 in between the two radio components, and hence was classified as an AGN. The nearby source S829.2 is a relatively weak radio source (0.30 mJy) which coincides ($\theta \sim 1.5''$) with SWIRE4_J003251.87-433016.7.
- *Sources S923, S930, S930.1 and S926* These four sources lie within less than $2'$ of each other and form a striking quartet at first sight. Source S923 is without doubt a classical double-lobed radio galaxy with an integrated flux density of 5.9 mJy. The SWIRE source SWIRE4_J003042.10-432335.4 is located on the line connecting the peaks of the two constituent radio components C923 and C931 and is therefore identified as the infrared counterpart. Source S930 is an otherwise inconspicuous radio source with an infrared counterpart, SWIRE4_J003038.21-432305.9, within $0.28''$. The naturally weighted image indicates a faint bridge of emission between components C930 and C941, hence both components have been grouped into S930. It blends with source S930.1, which consists of the two faint radio components C930.1 and C930.2 with integrated flux densities of 0.47 mJy and 0.55 mJy, respectively. In between components C930.1 and C930.2 is a very faint, uncatalogued infrared source, and thus the radio morphology together with the location of the IR source indicates that this is a double-lobed radio galaxy. Source S655 has a relatively bright IR counterpart (SWIRE4_J003035.03-432341.6) centred on the brighter one of its two radio components C926 and C926.1, with 2.7 mJy and 0.93 mJy, respectively. Unlike in sources S923 and S930.1, the IR source is centred on one of its constituents, but it was deemed more likely that both C926 and C926.1 are associated with this source rather than to postulate that C926 is

the radio counterpart to SWIRE4_J003035.03-432341.6 and that C926.1 is a separate source with no IR counterpart.

- *Sources S1189 and S1197* Source S1189 is a beautifully extended, large radio source. The number of constituent radio components is somewhat arbitrary, but there exists a low-SNR bridge of emission which connects the main part of the source and component C1212, 2' north, as well as many more low-SNR patches in between. The brightest part of S1189 is centred on SWIRE4_J003427.54-430222.5 (separation 0.75''), which we therefore identify as IR counterpart, and which has the morphology of an elliptical galaxy in optical images. Source S1197, 0.60'' from SWIRE4_J003419.55-430151.7, is unlikely to be connected to S1189. S1189 has the shape and extent of Wide-Angle Tail galaxies (WAT, Miley 1980) such as NGC 1265 (Owen et al. 1978). Their characteristic C-shape is believed to be caused by ram pressure against the jets while the galaxy is moving through the intracluster medium. The jets in S1189 are strongly bent backwards and almost touch another at the far ends. This is illustrated in Figure 10, where we have drawn contours beginning at 2σ to emphasize the effect. WAT radio sources can be used as cluster signposts (e.g., Blanton et al. 2003), but there is no known cluster at the position of S1189, although there is a little overdensity of galaxies at 115'' to its south-west, centred on a bright galaxy with elliptical morphology. The source is in the SUMSS catalogue with a flux density of 36.2 mJy, compared to a 1.4 GHz flux density of 45.0 mJy. However, it is clearly extended in the SUMSS image and not well represented by a Gaussian. Integrating over the source area in the SUMSS image yielded a total flux density of 51 mJy, and hence a spectral index of $\alpha = -0.25$.
- *Source S1192* This source is an example of a triple radio galaxy. It consists of the three components C1192, C1192.1, and C1192.2 with mJy flux densities. The brightest component, C1192.1, is centred on the IR source SWIRE4_J003320.68-430203.6. The other two components are several arcsec away from the nearest IR sources, and the overall morphology thus indicates that this is a bent triple radio galaxy. It therefore also could be a WAT.
- *Source S773* Source S773 is a rather faint radio source with $S_{20\text{cm}} = 0.37$ mJy, but it has a very bright infrared counterpart with $S_{24\mu\text{m}} = 28$ mJy within 0.72'', and is one of the few objects clearly visible in the SWIRE 70 μm image. Its unusual ratio of $\log_{10}(S_{24\mu\text{m}}/S_{20\text{cm}}) = 1.89$ lets it clearly stand out in Figure 7 as a separated dot in the bottom right corner. It has been classified by La Franca et al. (2004) as a type 1 AGN (based on optical line widths in excess of 1200 km/s) at redshift 0.143. Furthermore, it is one of the brightest X-ray sources found by Alexander et al. (2001) in a *BeppoSAX* survey of the ELAIS-S1 region.

- *Source S1081* Source S1081 is a very extended ($B_{\text{maj}} = 93''$), low-surface brightness source. Nevertheless, its integrated flux density is 2.4 mJy, and there is no obvious association with any one of the many nearby infrared sources. It is unlikely to be a sidelobe, as this region of the image is very good and free of artefacts. Furthermore, its extent indicates that it is not a noise spike, which would have a similar size as the restoring beam. We have convolved the radio image of Gruppioni et al. (1999) with a $1'$ restoring beam, to increase its sensitivity to extended structures, but their image was not sensitive enough to confirm or refute the reality of S1081. The nature of this object is unclear: given its size and the lack of a strong component it could be a cluster radio relic. Such objects are interpreted as leftovers of cluster mergers.

7. The radio-infrared relation

One of the goals of the ATLAS project is to trace the radio-infrared relation to very faint flux levels, to determine whether the relation exists in the early universe. Using *Spitzer* and VLA observations of the First Look Survey (Condon et al. 2003), Appleton et al. (2004) have determined a value of $q_{24} = \log(S_{24\mu\text{m}}/S_{20\text{cm}}) = 0.84 \pm 0.23$. Here, we note that Boyle et al. (2007) have employed a statistical analysis of the ELAIS-S1 radio image at the known positions of SWIRE sources. They find $q_{24} = 1.46$ using the observations presented here, and exactly the same value of q_{24} using the CDFS observations of Norris et al. (2006). Boyle et al. (2007) present an extensive description of the analysis and of simulations, and we refer the reader to their paper for details. We note, however, that the discrepancy of the value of q_{24} found by Appleton et al. (2004) and Boyle et al. (2007) remains unresolved.

We plot in Figure 9 a histogram of all individual values of q_{24} where $24\mu\text{m}$ fluxes were available, without k-correction. We also indicate on the diagram the distribution (also without k-correction) found by Appleton et al. (2004). We note that these authors also presented a k-correction for their data, but it was too small to reconcile their result with the result by Boyle et al. (2007). The tail towards lower values of q_{24} can be explained as arising from AGN, which have a radio excess and so do not obey the radio-infrared relation. Conversely, the sharp cutoff of the histogram at q_{24} is caused by a lack of objects with an infrared excess. This is expected when one interprets the infrared emission as arising from star formation, which in turn generates radio emission according to the radio-infrared relation. Appleton et al. (2004) excluded AGN based on spectroscopic observations and thus their sample is not contaminated by AGN, and they do not see the tail towards low values of q_{24} .

We note that the distribution of q_{24} found by Norris et al. (2006) has a different shape

than ours. It is rather constant between $q_{24} = -0.5$ and $q_{24} = 1.5$, and indicates a double-peaked distribution. However, the differences in sensitivity make it impossible to construct similar samples from the CDFS data presented by Norris et al. (2006) and the data presented here. We therefore postpone a detailed analysis of the distribution of q_{24} to the time when the ATLAS survey is complete.

8. Conclusions

We have presented the first data from the ATLAS observations of the ELAIS-S1 region, and a list of 1276 radio sources extracted from the image. Radio sources have been matched to infrared SWIRE sources and been classified as AGN if the morphology, radio-to-infrared ratio, or the literature indicated so. We discover another 31 Infrared-Faint Radio Sources, bringing the total number of these objects found with the ATLAS survey to 55, and find no significant difference between the distribution of source flux densities between the ELAIS-S1 and the CDFS at $S_{20\mu\text{m}} > 0.3$ mJy. We find a distribution of $q_{24} = \log(S_{20\mu\text{m}}/S_{20\text{cm}})$ which is in broad agreement with the distribution found by Appleton et al. (2004). No further interpretation of our data is presented, partly because other essential information such as redshifts is not yet available and partly because the observations are not yet complete.

The Australia Telescope Compact Array is operated by the CSIRO Australia Telescope National Facility. IRS acknowledges support from the Royal Society. This research has made extensive use of the NASA/IPAC Extragalactic Database (NED) which is operated by the Jet Propulsion Laboratory, California Institute of Technology, under contract with the National Aeronautics and Space Administration.

REFERENCES

- Alexander, D. M., La Franca, F., Fiore, F., et al. 2001, *ApJ*, 554, 18
- Appleton, P. N., Fadda, D. T., Marleau, F. R., et al. 2004, *ApJS*, 154, 147
- Becker, R. H., White, R. L., & Helfand, D. J. 1995, *ApJ*, 450, 559
- Berta, S., Rubele, S., Franceschini, A., et al. 2006, *A&A*, 451, 881
- Bertin, E. & Arnouts, S. 1996, *A&AS*, 117, 393

- Blanton, E. L., Gregg, M. D., Helfand, D. J., Becker, R. H., & White, R. L. 2003, *AJ*, 125, 1635
- Bock, D. C.-J., Large, M. I., & Sadler, E. M. 1999, *AJ*, 117, 1578
- Boyle, B. J., Cornwell, T. J., Middelberg, E., et al. 2007, *MNRAS*, accepted
- Colless, M., Dalton, G., Maddox, S., et al. 2001, *MNRAS*, 328, 1039
- Condon, J. J. 1997, *PASP*, 109, 166
- Condon, J. J., Cotton, W. D., Yin, Q. F., et al. 2003, *AJ*, 125, 2411
- Gruppioni, C., Ciliegi, P., Rowan-Robinson, M., et al. 1999, *MNRAS*, 305, 297
- Higdon, J. L., Higdon, S. J. U., Weedman, D. W., et al. 2005, *ApJ*, 626, 58
- Jones, D. H., Saunders, W., Colless, M., et al. 2004, *MNRAS*, 355, 747
- La Franca, F., Gruppioni, C., Matute, I., et al. 2004, *AJ*, 127, 3075
- Lonsdale, C. J., Smith, H. E., Rowan-Robinson, M., et al. 2003, *PASP*, 115, 897
- Maddox, S. J., Efstathiou, G., Sutherland, W. J., & Loveday, J. 1990, *MNRAS*, 243, 692
- Magliocchetti, M., Maddox, S. J., Lahav, O., & Wall, J. V. 1998, *MNRAS*, 300, 257
- Middelberg, E. 2006, *Publications of the Astronomical Society of Australia*, 23, 64
- Miley, G. 1980, *ARA&A*, 18, 165
- Norris, R. P., Afonso, J., Appleton, P. N., et al. 2006, *AJ*, 132, 2409
- Norris, R. P., Tingay, S. J., Phillips, C., et al. 2007, *MNRAS*
- Oliver, S., Rowan-Robinson, M., Alexander, D. M., et al. 2000, *MNRAS*, 316, 749
- Owen, F. N., Burns, J. O., & Rudnick, L. 1978, *ApJ*, 226, L119
- Puccetti, S., Fiore, F., D’Elia, V., et al. 2006, *A&A*, 457, 501
- Ricci, R., Sadler, E. M., Ekers, R. D., et al. 2004, *MNRAS*, 354, 305
- Sault, R. J., Teuben, P. J., & Wright, M. C. H. 1995, in *ASP Conf. Ser. 77: Astronomical Data Analysis Software and Systems IV*, 433
- Schinnerer, E., Carilli, C. L., Scoville, N. Z., et al. 2004, *AJ*, 128, 1974

- Serjeant, S., Efstathiou, A., Oliver, S., et al. 2001, MNRAS, 322, 262
- Shethman, S. A., Landy, S. D., Oemler, A., et al. 1996, ApJ, 470, 172
- Skrutskie, M. F., Cutri, R. M., Stiening, R., et al. 2006, AJ, 131, 1163
- Vanzella, E., Cristiani, S., Dickinson, M., et al. 2005, A&A, 434, 53
- Wegner, G., Bernardi, M., Willmer, C. N. A., et al. 2003, AJ, 126, 2268

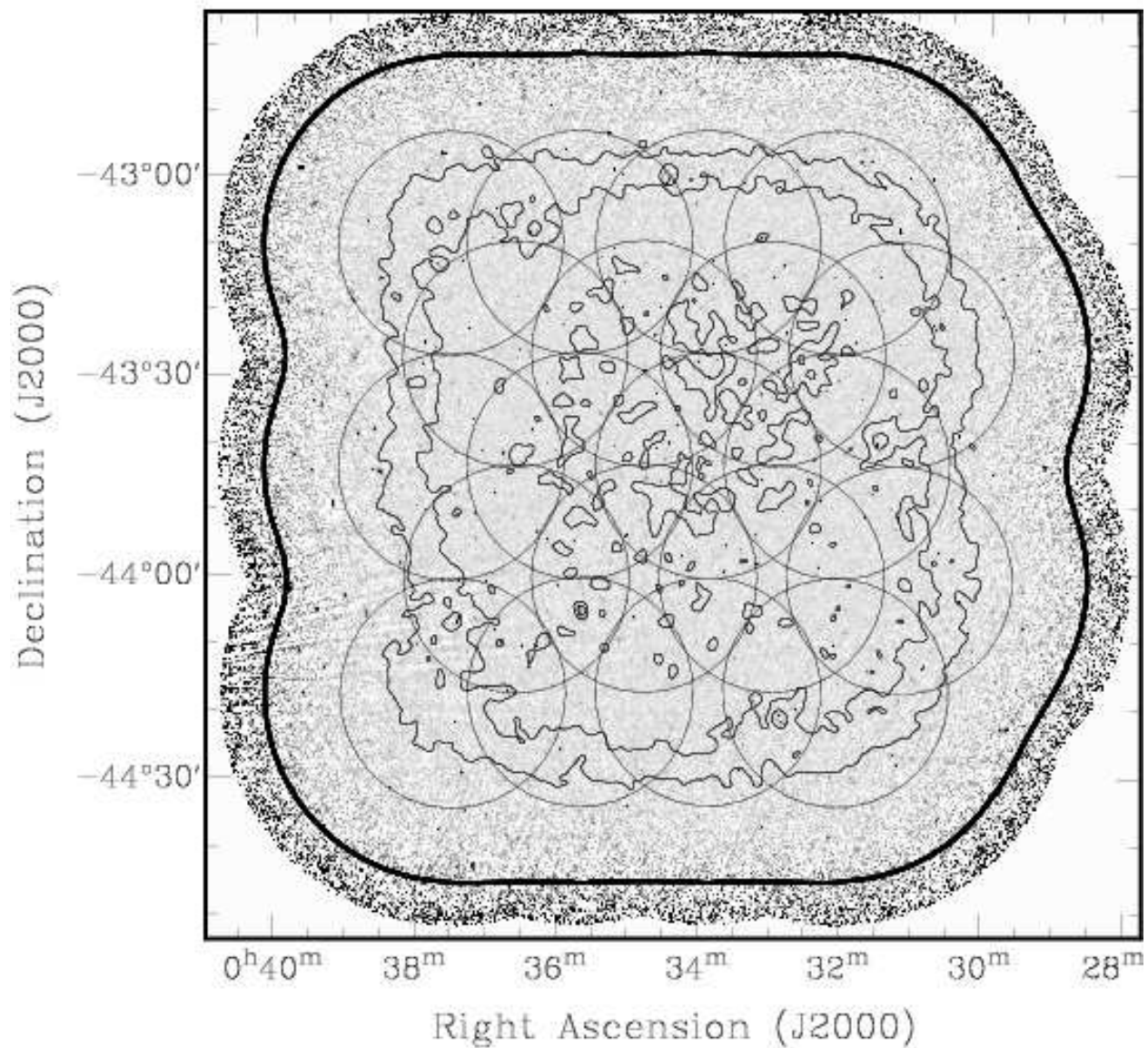


Fig. 1.— An overview of the observed area. The circles indicate the 20 antenna pointings and the FWHM of the primary beams. The thin contours show noise levels of $25 \mu\text{Jy}$, $35 \mu\text{Jy}$, and $45 \mu\text{Jy}$, as calculated by SExtractor (Bertin & Arnouts 1996). The thick contour indicates where the predicted sensitivity is $250 \mu\text{Jy}$ and marks the area which we have analysed. The image has been clipped where the response of the antenna primary beams has dropped to below 3% of its peak value.

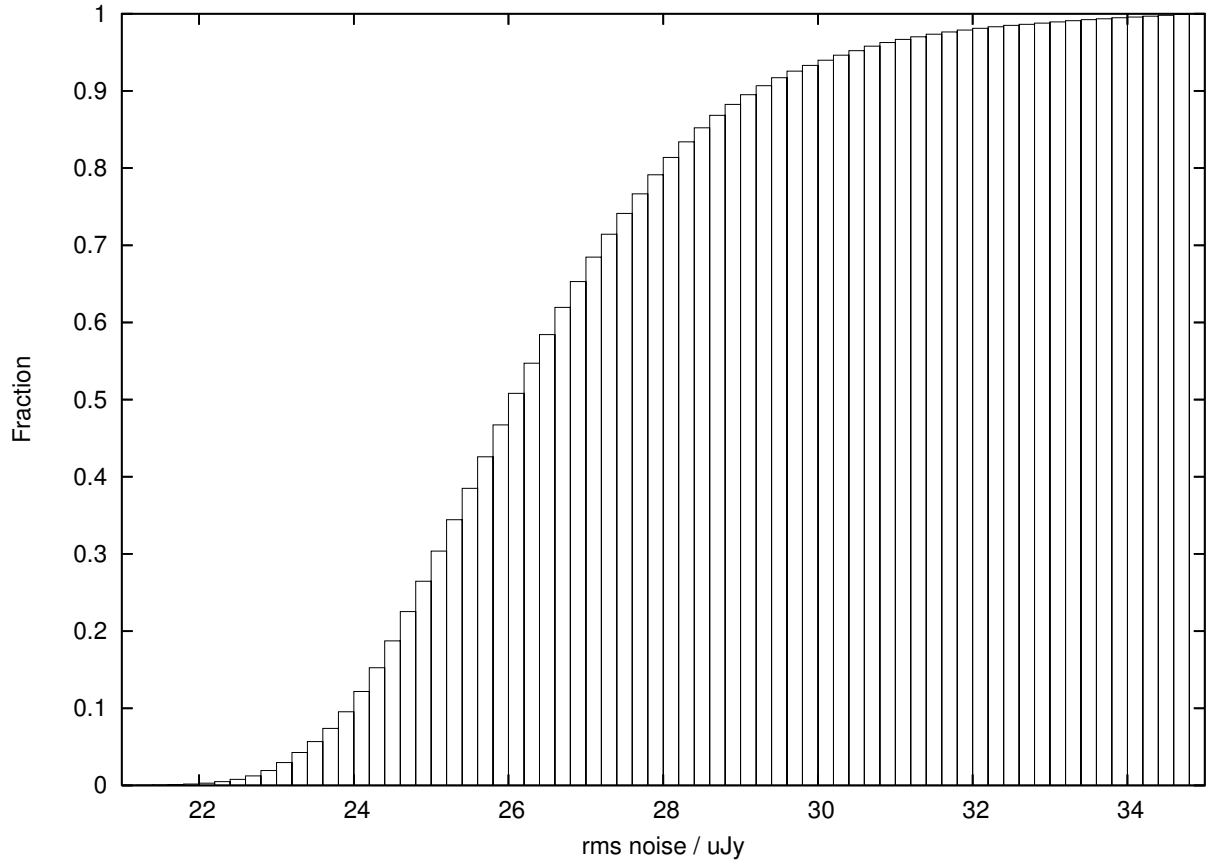


Fig. 2.— Cumulative histogram of the pixel values of the rms map in the central 1 deg^2 of the observed area.

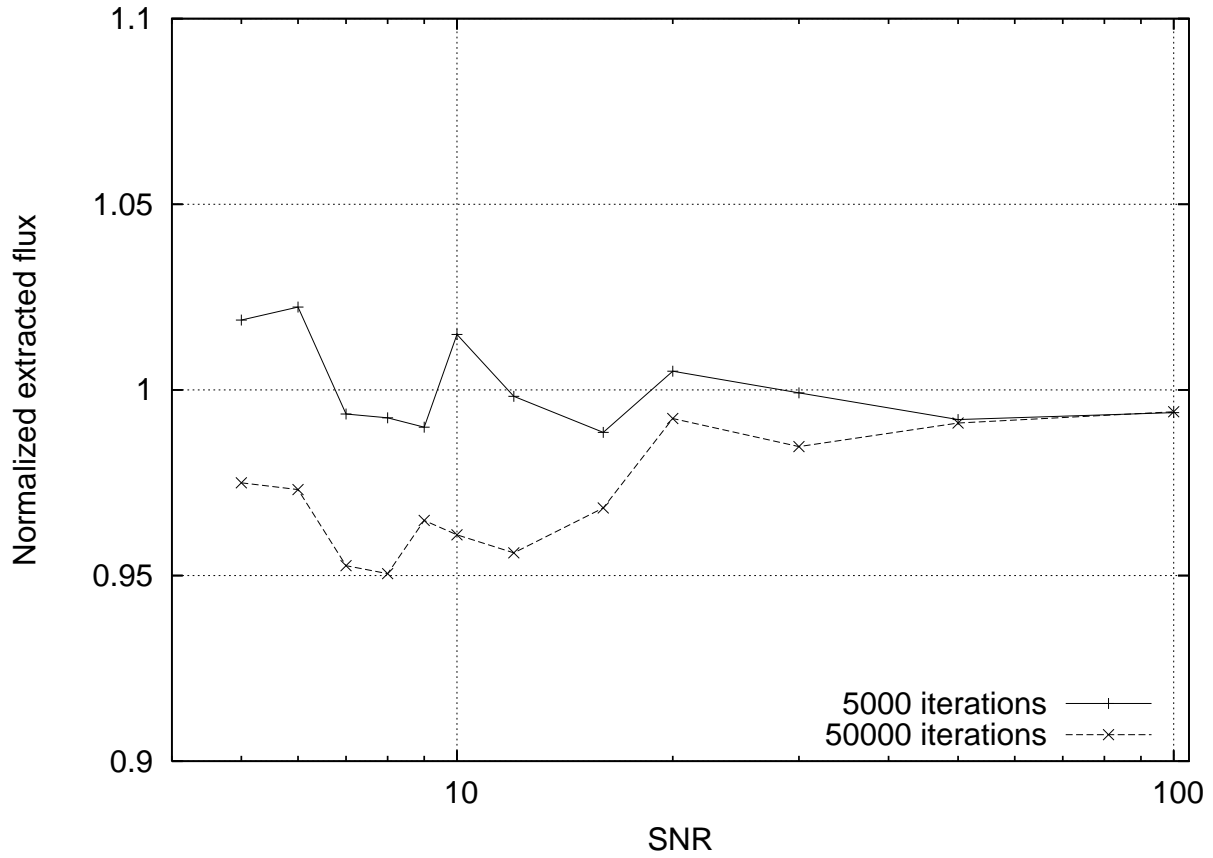


Fig. 3.— Results from our tests for clean bias. Shown is the median normalized flux of sources extracted from simulated images as a function of SNR. Using 5000 iterations in cleaning does not produce a significant clean bias, but using 50000 iteration does, although the bias is comparatively small.

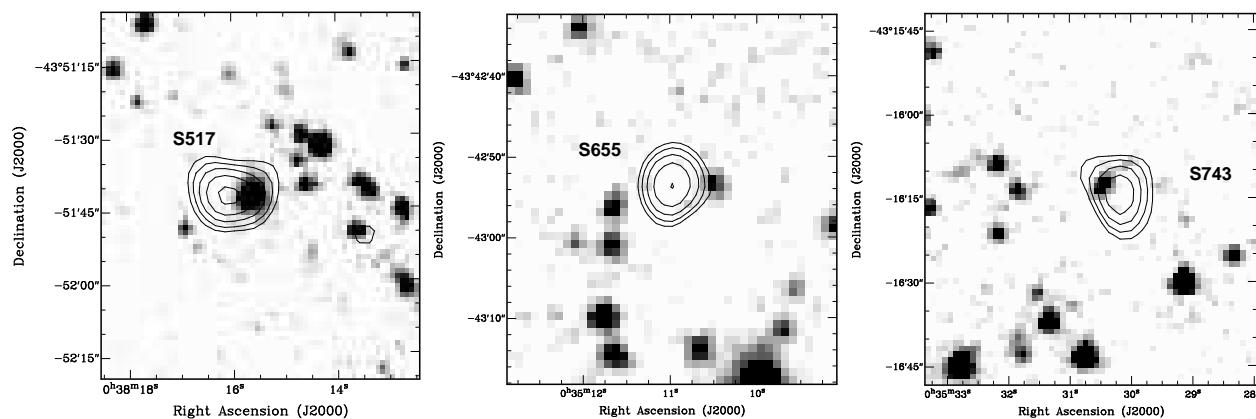


Fig. 4.— Examples of sources with relatively large ($> 3''$) separations between the fitted radio position and the catalogued SWIRE position. Shown are the radio SNR contours from SNR=4 and increasing by factors of $\sqrt{2}$, superimposed on the SWIRE $3.6 \mu\text{m}$ image as greyscale. *Left:* S517 is strong and clearly extended towards SWIRE4_J003815.62-435142.0, which was deemed to be associated despite a separation of $4.4''$. *Middle:* Source S655 is separated by $5.3''$ from its SWIRE counterpart. Shown here is a portion of the radio image made with super-uniform weighting, and hence higher resolution, which shows the extension clearly. *Right:* Source S1034 is similarly extended towards a SWIRE source, with a separation of $3.4''$.

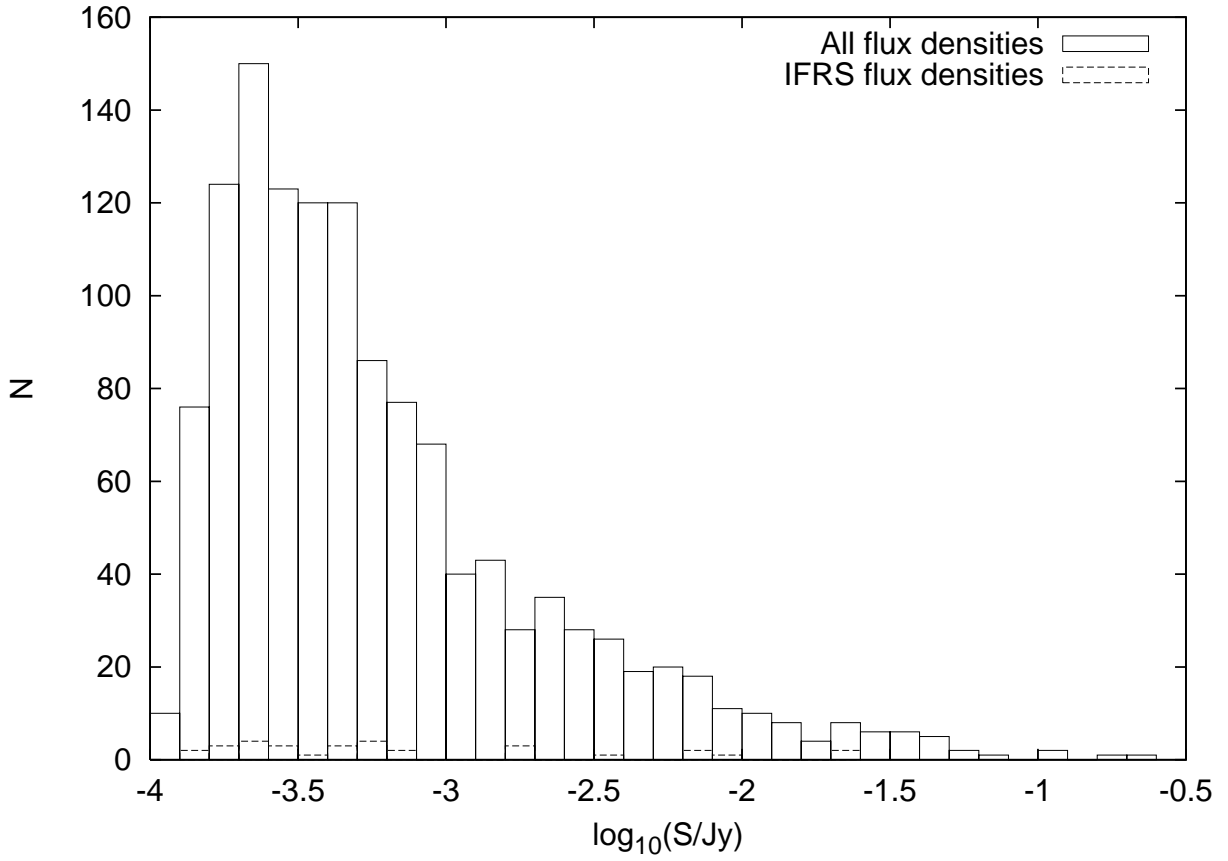


Fig. 5.— A histogram of the integrated flux densities of the sources in our survey. A histogram of the IFRS flux densities is drawn with dashed lines.

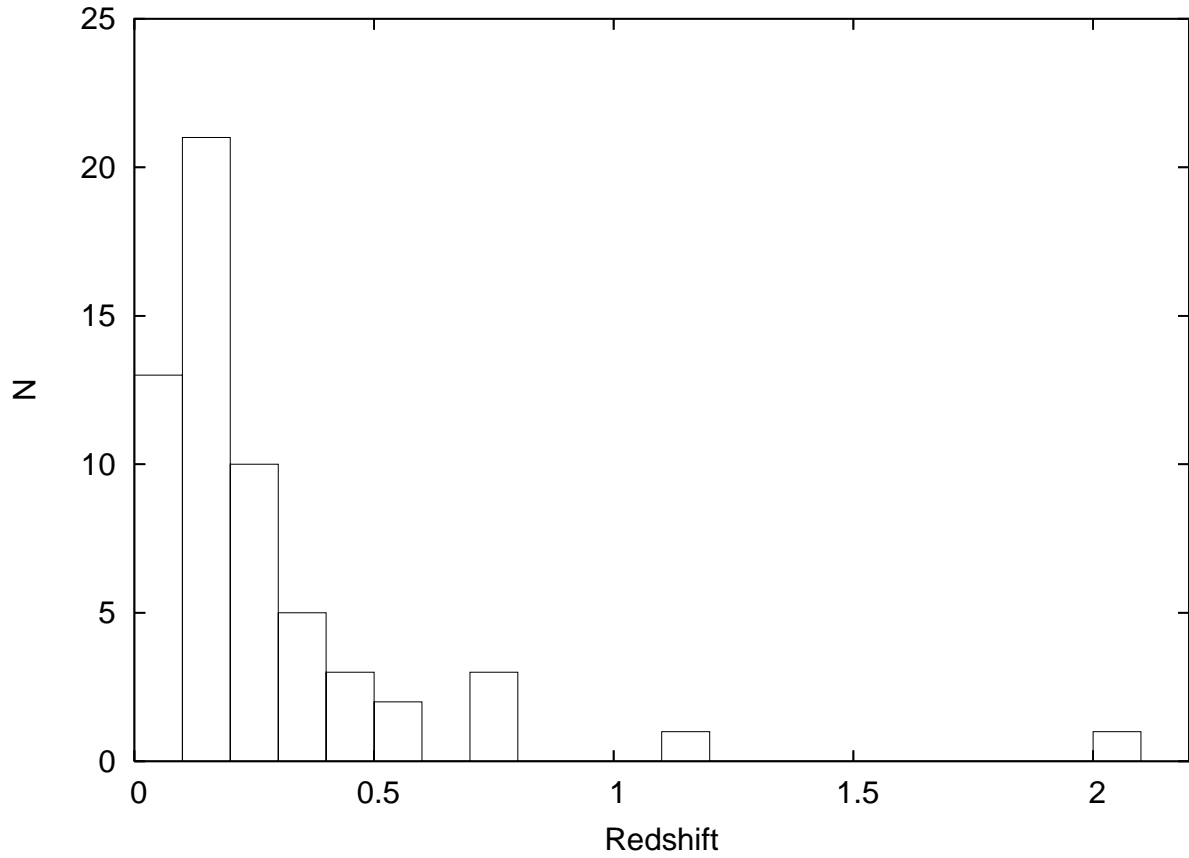


Fig. 6.— A histogram of the 59 redshifts available for objects in our catalogue, taken from the literature. There is no hint of large-scale structure, but this may be hidden by too few data points.

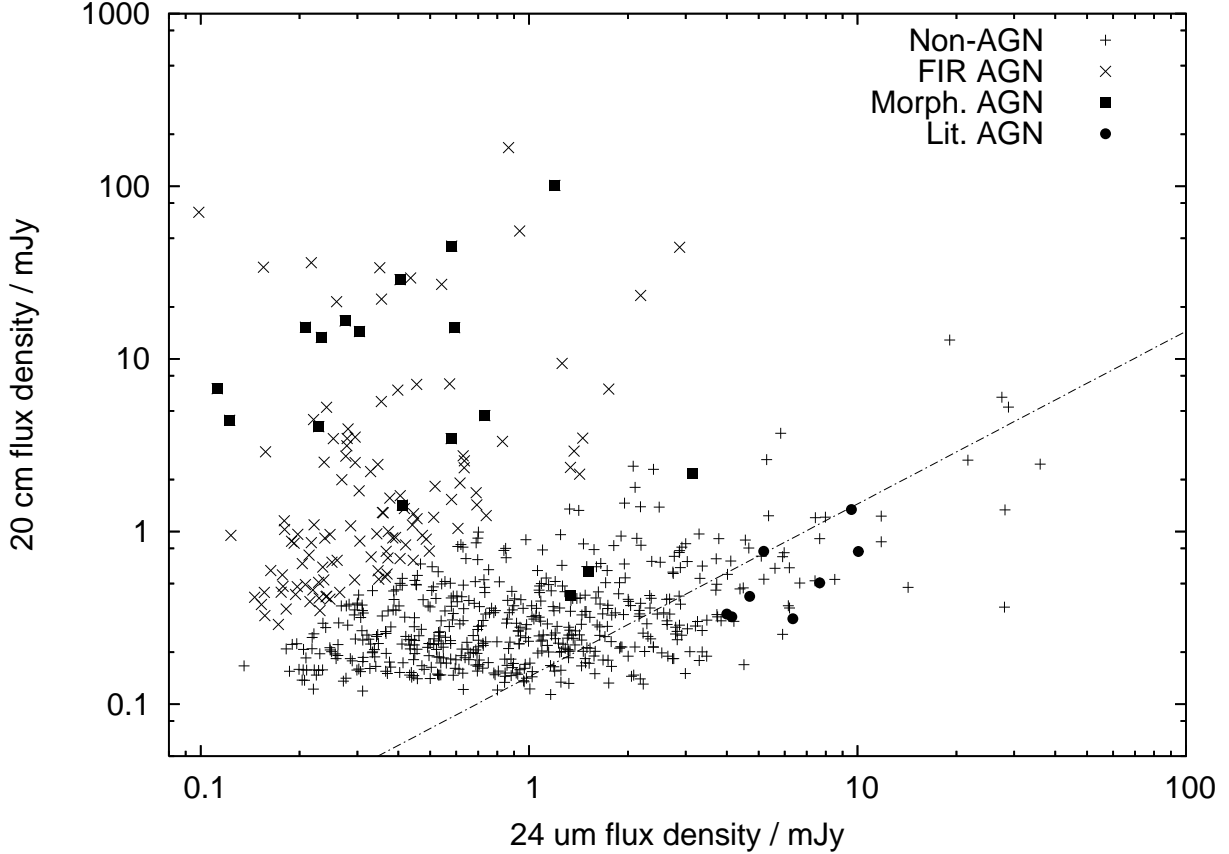


Fig. 7.— 20 cm vs. $24\ \mu\text{m}$ flux densities of all sources, with AGN plotted separately. Symbols indicate the type of AGN classification: pluses show non-AGN; crosses indicate AGN classified based on an 10-fold excess of radio emission compared to the infrared-radio emission derived by Appleton et al. (2004); filled squares indicate AGN classified based on their radio morphology; and filled circles indicate sources classified as AGN in the literature. The line indicates $q_{24} = \log(S_{24\mu\text{m}}/S_{20\text{cm}}) = 0.84$ found by Appleton et al. (2004). The flattening of the distribution towards lower values of $S_{24\mu\text{m}}$ is caused by the limited sensitivity of the radio observations, which at low $24\ \mu\text{m}$ flux densities are only able to pick up objects with comparatively high radio flux densities. For a detailed analysis of the radio-infrared relation derived from the ELAIS-S1 radio and $24\ \mu\text{m}$ data, see Boyle et al. (2007).

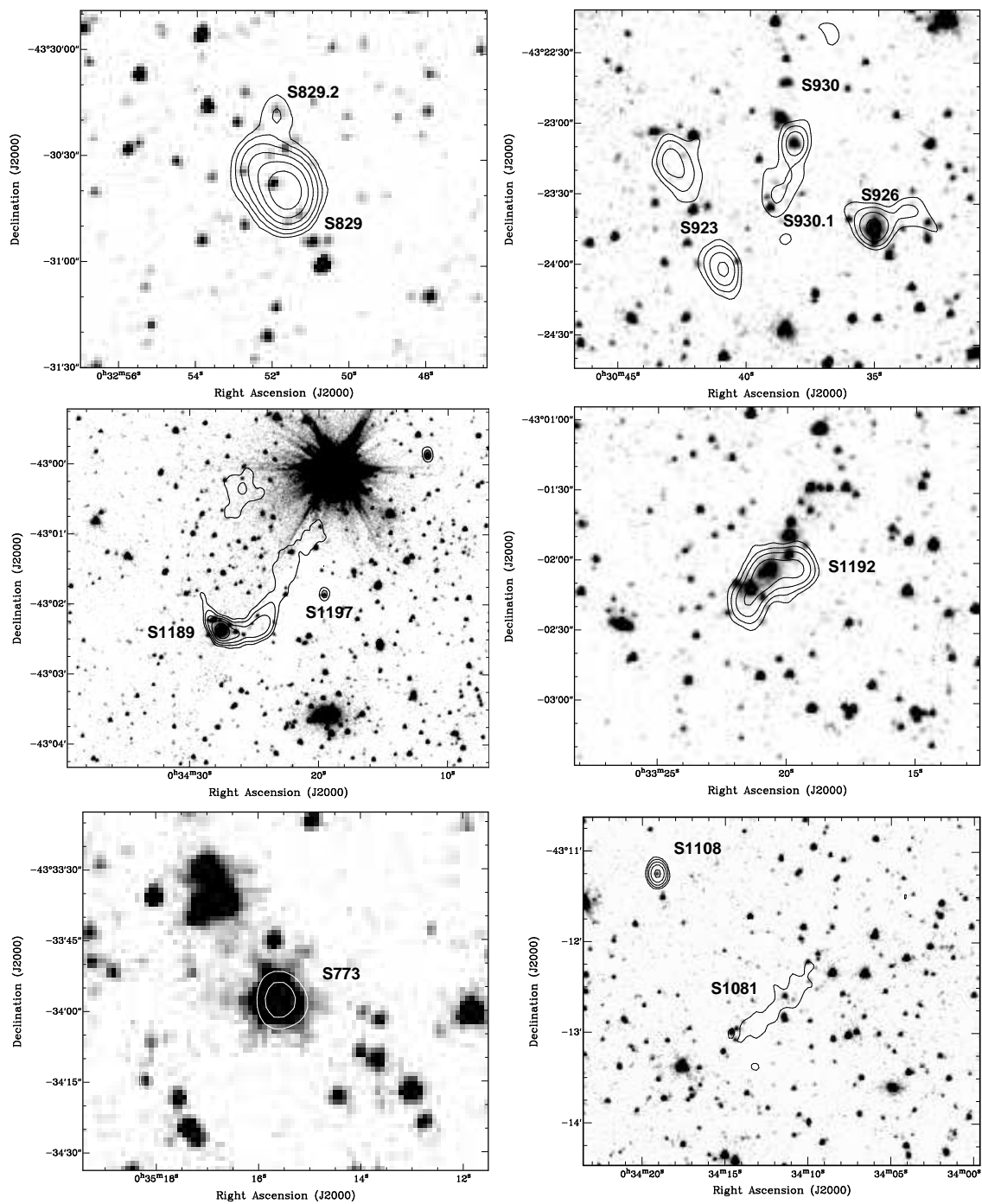


Fig. 8.— Six sample extracts from the radio image (contours), superimposed on the $3.6\ \mu\text{m}$ *Spitzer* image (greyscale). Contours start at $\text{SNR}=4$ and increase by factors of two. The rms in the images is $27\ \mu\text{Jy}$ (top left), $46\ \mu\text{Jy}$ (top right), $49\ \mu\text{Jy}$ (middle left), $43\ \mu\text{Jy}$ (middle right), $29\ \mu\text{Jy}$ (lower left), and $28\ \mu\text{Jy}$ (lower right). See the text for a detailed description of these sources.

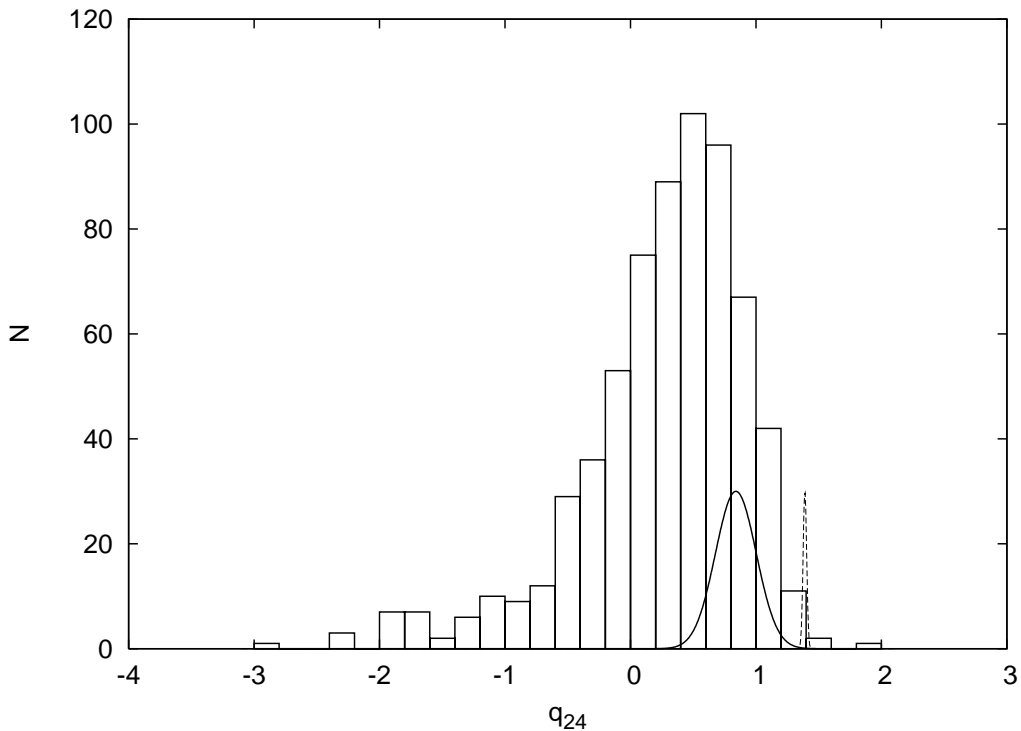


Fig. 9.— Histogram of q_{24} from all ELAIS-S1 data. The solid Gaussian indicates $q_{24} = 0.84 \pm 0.23$ as found by Appleton et al. (2004), and the dashed Gaussian $q_{24} = 1.39 \pm 0.02$ as found by Boyle et al. (2007). The histogram peak is in broad agreement with the Appleton et al. (2004) results, and the tail towards low values of q_{24} is caused by AGN, which are included in our data but were discarded by Appleton et al. (2004). Why the Boyle et al. (2007) peak does not agree with the histogram and the Appleton et al. (2004) distribution is not understood.

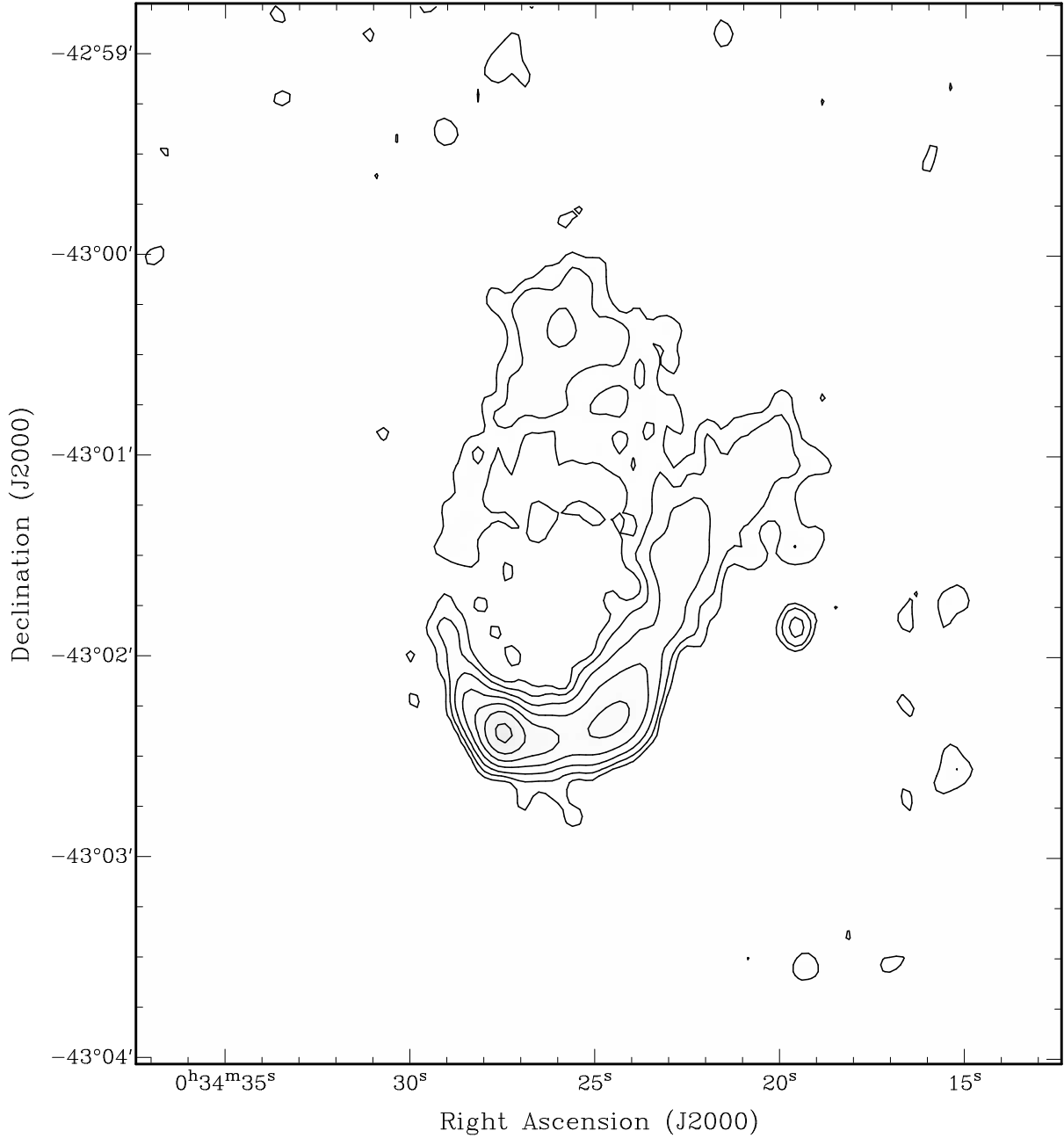


Fig. 10.— Source S1189, drawn with contours starting at $2\sigma = 70 \mu\text{Jy}$ and increasing by factors of two. The two jets are strongly bent backwards, and their far ends almost touch each other. The morphology suggests that the source is moving through a relatively dense medium, indicating the presence of a yet unknown galaxy cluster.

Date	Config	Int. time hours
(1)	(2)	(3)
09,10,11 Jan 04	6A	8.91, 8.77, 6.99
30 Jan 04, 01 Feb 04	6B	9.11, 9.47
19, 27 Dec 04; 01, 02, 03 Jan 05	1.5D	3.82, 9.09, 9.89, 8.41, 8.97
09, 10, 11, 20, 21, 22 Jan 05	750B	9.69, 9.51, 10.59, 4.15, 8.74, 7.29
25 Mar 05; 08, 11 Apr 05	6A	8.9, 9.23, 9.02
24, 26, 30 Apr 05; 01 May 05	750A	8.16, 8.9, 8.74, 8.53
08, 09 Jun 05	EW367	9.28, 9.05
19, 24 Jun 05	6B	9.17, 9.3

Table 1: Observing dates, array configurations and net integration times on ELAIS-S1 pointings.

Source / Pointing	RA	Dec
(1)	(2)	(3)
1934-638	19:39:25.02	-63:42:45.62
0022-423	0:24:42.99	-42:02:03.95
1	0:32:03.55	-43:44:51.24
2	0:31:10.95	-43:27:59.64
3	0:32:05.04	-43:11:18.84
4	0:33:51.29	-43:11:24.96
5	0:32:57.67	-43:28:09.00
6	0:33:50.79	-43:44:57.36
7	0:35:38.02	-43:44:57.36
8	0:34:44.40	-43:28:11.88
9	0:35:37.51	-43:11:24.96
10	0:37:23.76	-43:11:18.84
11	0:36:31.13	-43:28:09.00
12	0:37:25.25	-43:44:51.24
13	0:36:31.13	-44:01:42.84
14	0:37:25.25	-44:18:34.44
15	0:35:38.02	-44:18:34.44
16	0:34:44.40	-44:01:42.84
17	0:32:57.67	-44:01:42.84
18	0:33:50.79	-44:18:34.44
19	0:32:03.55	-44:18:34.44
20	0:31:10.95	-44:01:42.84

Table 2: Coordinates of the calibrators and the pointings depicted in Figure 1.

Separation	N	m	%
(1)	(2)	(3)	
$< 1''$	656	16	2.4
$1'' - 2''$	350	20	4.2
$2'' - 3''$	86	9	10.5
$> 3''$	45	-	-

Table 3: Summary of the upper limits on the number of false cross-identifications. Column 1 gives the separation, column 2 the number of sources within this range, column 3 the number of radio sources likely to be wrongly cross-identified with infrared sources, and column 4 gives this number as a percentage.

Table 4. Radio component data

	Name	RA	Dec	RA err	Dec err	Peak	err	Int	err	rms	B_{maj}	B_{min}	PA
(1)	(2)	(3)	(4)	arcsec (5)	arcsec (6)	mJy (7)	mJy (8)	mJy (9)	mJy (10)	μJy (11)	arcsec (12)	arcsec (13)	$^{\circ}$ (14)
C75	ATELAIS J003419.30-442647.2	00:34:19.308302	-44:26:47.213520	0.33	0.23	0.25	0.03	0.25	0.01	31	10.26	7.17	0
C76	ATELAIS J003247.08-442628.8	00:32:47.088391	-44:26:28.830840	0.20	0.16	0.39	0.04	1.02	0.03	42	16.73	11.48	151
C77	ATELAIS J003138.76-442620.6	00:31:38.765112	-44:26:20.670360	0.16	0.12	0.35	0.04	0.35	0.01	39	10.26	7.17	0
C78	ATELAIS J003152.54-442620.6	00:31:52.548125	-44:26:20.666040	0.14	0.10	0.40	0.04	0.40	0.01	40	10.26	7.17	0
C79	ATELAIS J003248.60-442625.7	00:32:48.606058	-44:26:25.750680	0.38	0.26	0.31	0.04	0.31	0.02	42	10.26	7.17	0
C80	ATELAIS J003659.30-442622.2	00:36:59.305858	-44:26:22.295400	0.26	0.29	0.17	0.04	0.37	0.02	40	14.09	10.97	126
C81	ATELAIS J003320.05-442617.8	00:33:20.053469	-44:26:17.850480	0.09	0.07	0.42	0.04	0.47	0.01	39	10.79	7.63	21
C82	ATELAIS J003832.11-442540.6	00:38:32.113102	-44:25:40.639080	0.12	0.08	1.26	0.06	1.26	0.02	62	10.26	7.17	0
C83	ATELAIS J003052.17-442537.3	00:30:52.170276	-44:25:37.398360	0.28	0.20	0.29	0.05	0.48	0.02	55	15.14	7.89	30
C84	ATELAIS J003253.48-442543.5	00:32:53.487876	-44:25:43.583880	0.09	0.06	0.39	0.03	0.56	0.01	36	12.66	8.35	2
C85	ATELAIS J003836.66-442513.5	00:38:36.662047	-44:25:13.595520	0.06	0.05	1.66	0.06	2.57	0.03	67	12.04	9.46	165
C86	ATELAIS J003602.72-442539.8	00:36:02.721341	-44:25:39.837720	0.06	0.05	1.31	0.04	1.50	0.02	40	10.56	7.99	177
C87	ATELAIS J003757.04-442516.6	00:37:57.045794	-44:25:16.619160	0.41	0.29	0.28	0.04	0.28	0.02	44	10.26	7.17	0
C88	ATELAIS J003543.38-442534.9	00:35:43.389367	-44:25:34.921200	0.24	0.15	0.20	0.04	0.20	0.01	38	10.26	7.17	0
C89	ATELAIS J003215.03-442521.8	00:32:15.038647	-44:25:21.858960	0.24	0.22	0.21	0.03	0.29	0.02	37	10.97	9.24	152

Note. — A section of the table with component data. Table 4 is published in its entirety in the electronic edition of the *Astronomical Journal*. A portion is shown here for guidance regarding its form and content. *Column 1*: a component number we use in this paper. In some cases, sources were split up into sub-components, resulting in component numbers such as “C5” and “C5.1”. However, this is no anticipation of the grouping of components to sources, which was carried out independently; *column 2*: designation for this component. In the case of single-component sources, this is identical to the source name used in table 5. This is the formal IAU designation and should be used in the literature when referring to this component; *columns 3/4*: right ascension and declination (J2000.0); *columns 5/6*: uncertainties in Right Ascension and Declination. These include the formal uncertainties derived from the Gaussian fit together with a potential systematic error in the position of the calibrator source of 0.1 arcsec; *columns 7/8*: peak flux density at 20 cm (in mJy) of the fitted Gaussian component, and the associated error as described in the text; *columns 9/10*: integrated flux density at 20 cm (in mJy) of the fitted Gaussian component, and the associated error; *column 11*: the value (in μJy) of the rms map generated by SExtractor at the position of the component; *columns 12/13/14*: the FWHM of the major and minor axes of the Gaussian in arcsec, and its position angle in degrees.

Table 4. Radio component data (continued)

	Dec. Peak mJy	Dec. B_{maj} arcsec	Dec. B_{min} arcsec	Dec. PA °	sidelobe?
(1)	(15)	(16)	(17)	(18)	(19)
C75					
C76	0.68	13.82	7.99	141	
C77					
C78					
C79					
C80	0.44	11.61	5.25	112	*
C81					
C82					
C83					
C84	1.3	7.43	4.27	4	
C85	5.21	7.27	4.99	129	
C86	13.12	3.64	2.30	108	
C87					
C88					
C89	2.15	6.85	1.45	110	

Note. — Radio component data (continued). *Column 15*: the deconvolved peak flux density of the component in mJy. If the undeconvolved fitted major or minor axis size was within one formal standard error of the restoring beam size, no value is given; *columns 16/17/18*: the deconvolved FWHM major and minor axes of the Gaussian in arcsec, and its position angle in degrees. If the undeconvolved fitted major or minor axis size was within one formal standard error of the restoring beam size, no value is given; *column 19*: an asterisk in this column indicates that this component was deemed to be a sidelobe.

Table 5. Radio source data

	Name	Comp.	RA	Dec	SWIRE source	$S_{20\text{cm}}$ mJy	$\Delta S_{20\text{cm}}$ mJy
(1)	(2)	(3)	(4)	(5)	(6)	(7)	(8)
S693	ATELAIS J003320.72-434030.1	C693	00:33:20.72	-43:40:30.11	SWIRE4_J003320.74-434030.1	0.38	0.05
S694	ATELAIS J003020.95-433942.8	C694	00:30:20.95	-43:39:42.89	SWIRE4_J003020.97-433942.7	49.58	2.48
S695	ATELAIS J003414.72-434030.7	C695	00:34:14.72	-43:40:30.74		0.15	0.03
S696	ATELAIS J003402.27-434008.6	C696	00:34:02.27	-43:40:08.60	SWIRE4_J003402.20-434014.8	0.49	0.04
S697	ATELAIS J003841.55-433925.0	C697, C697.1	00:38:41.55	-43:39:25.06	SWIRE4_J003841.54-433925.0	13.32	0.67
S698	ATELAIS J003412.39-434005.8	C698	00:34:12.39	-43:40:05.84	SWIRE4_J003412.32-434005.2	0.16	0.03
S699	ATELAIS J003513.86-433959.1	C699	00:35:13.86	-43:39:59.19	SWIRE4_J003513.86-433959.0	0.33	0.04
S700	ATELAIS J003703.48-433935.5	C700	00:37:03.48	-43:39:35.56	SWIRE4_J003703.00-433935.3	0.41	0.06
S701	ATELAIS J003141.08-433917.2	C701	00:31:41.08	-43:39:17.22	SWIRE4_J003141.18-433916.8	0.50	0.07
S702	ATELAIS J003038.12-433903.8	C702, C710	00:30:38.12	-43:39:03.89	SWIRE4_J003038.11-433903.8	1.48	0.10
S703	ATELAIS J003616.52-433917.5	C703	00:36:16.52	-43:39:17.55	SWIRE4_J003616.54-433918.3	13.83	0.69
S704	ATELAIS J003544.33-433930.2	C704	00:35:44.33	-43:39:30.25	SWIRE4_J003544.38-433930.4	0.22	0.04
S705	ATELAIS J003517.65-433931.9	C705	00:35:17.65	-43:39:31.97	SWIRE4_J003517.66-433931.0	0.18	0.03
S706	ATELAIS J003815.05-433906.5	C706	00:38:15.05	-43:39:06.53	SWIRE4_J003814.95-433907.5	0.34	0.07
S707	ATELAIS J003828.03-433847.2	C707, C713	00:38:28.03	-43:38:47.26	SWIRE4_J003828.02-433847.2	6.00	2.44

Note. — A section of the table with radio source data. Table 5 is published in its entirety in the electronic edition of the *Astronomical Journal*. A portion is shown here for guidance regarding its form and content. *Column 1*: source number we use in this paper; *column 2*: designation for this source. In the case of single-component sources, this is identical to the component name used in Table 3. This is the formal IAU designation and should be used in the literature when referring to this source; *column 3*: components which are deemed to belong to this source; *columns 4/5*: right ascension and declination (J2000.0). In the case of single-component sources, this is the radio position of the component. In the case of multi-component sources with good infrared identification, the SWIRE position is used. In the case of multi-component sources without infrared identification, the coordinates are a flux-weighted mean of the components' coordinates; *column 6*: name of the SWIRE source; *columns 7/8*: integrated radio flux density of the source in mJy and the associated error. In the case of extended or multiple-component sources, the flux density has been integrated over the source region, rather than taking the sum of its constituent components

Table 5. Radio source data (continued)

(1)	$S_{3.6\mu\text{m}}$ μJy (9)	$S_{4.5\mu\text{m}}$ μJy (10)	$S_{5.8\mu\text{m}}$ μJy (11)	$S_{8.0\mu\text{m}}$ μJy (12)	$S_{24\mu\text{m}}$ μJy (13)	B mag (14)	V mag (15)	R mag (16)	AGN (17)	M (18)	z (19)	ref (20)	comment (21)
S693	253.94	275.32	281.19	561.27	2892.44	21.16	19.95	19.08					
S694	435.13	312.91	158.69	86.96									
S695													unclear XID
S696	7.22	13.64											IFRS
S697	155.47	103.93	94.40	49.86	233.13	22.39	21.53	20.51	mf	x/-			clearly a radio double, M-test fails due flux ratio of constituents
S698	20.21	27.24		186.36		24.68	24.78	24.04					
S699	2038.05	1476.46	844.10	639.00	156.85	18.02	16.65	15.99	f		0.11	6dF	
S700	39.99	26.94		247.30		22.69	22.04	21.23	f				
S701	145.32	83.23	58.80										
S702	64.81	57.32							m				extended, low surface brightness object, bridge of emission towards C710, which has no XID, hence core-jet morphology
S703	63.27	68.60	63.05			25.14							confused XID
S704	14.14	15.81				24.22	24.11	23.73					
S705	45.86	48.11	54.40	655.28		24.03	23.90						confused XID
S706	33.36	38.41	64.01	757.86		24.85	24.39	24.07					confused XID
S707	6277.45	4263.60	9520.63	40203.53	27526.39	15.81	15.22	14.71					C713 probably associated

Note. — Radio source data (continued). *Column 9-13*: flux density of the infrared counterpart in the four IRAC bands at $3.6\mu\text{m}$ – $8.0\mu\text{m}$ and in the MIPS band at $24\mu\text{m}$, in μJy . Aperture-corrected flux densities have been used unless the source was clearly extended, in which case the flux in a Kron aperture has been used; *column 14-16*: optical magnitude of the counterpart; *column 17*: flag indicating whether a source has been classified as AGN or not, and based on what criteria. An “f” indicates AGN classification based on the far-infrared-radio relation, an “m” based on morphology, and an “l” based on classification taken from the literature; *column 18*: result of the test developed by Magliocchetti et al. (1998) as described in the text, performed for double radio sources. A “-” indicates failure, a “x” success of the two parts of the test (separation and flux density ratio of the constituents); *column 19*: source redshift; *column 20*: reference for the redshift. The codes indicate the following publications: 2df - Colless et al. (2001), 6dF - Jones et al. (2004), A01 - Alexander et al. (2001), L04 - La Franca et al. (2004), P06 - Puccetti et al. (2006), S01 - Serjeant et al. (2001), S96 - Shectman et al. (1996), W03 - Wegner et al. (2003); *column 21*: comment

Table 5. Radio source data (continued)

(1)	G99 name (22)	other name (23)
S693	ELAIS20R_J003021-433943	
S694		
S695	ELAIS20R_J003402-434011	
S696	ELAIS20R_J003842-433924	
S697		
S698		2MASX J00351384-4339588
S699		
S700		
S701		
S702	ELAIS20R_J003617-433918	
S703		
S704		
S705		
S706	ELAIS20R_J003828-433849	ESO 242- G 021
S707		

Note. — Radio source data (continued). *Column 22*: The designation by Gruppioni et al. (1999); *column 23*: Other names obtained from NED

Source	SUMSS RA	SUMMS Dec	S mJy	Sep. arcsec	α	Comment
(1)	(2)	(3)	(4)	(5)	(6)	(7)
S207	00:30:48.60	-44:14:33.10	34.6	14.40	-1.06	S207, S207.2 and S212 all blend together in this source
S220	00:37:09.57	-44:14:08.40	11.6	2.18	-1.48	
S258	00:32:04.54	-44:11:32.70	59.0	2.36	-1.00	
S272	00:36:44.04	-44:10:54.90	13.3	2.53	-0.96	blends with S278
S293	00:29:25.72	-44:08:24.80	12.4	2.08	-1.11	blends with S304
S296	00:36:50.07	-44:08:59.70	14.7	3.00	-0.80	
S311	00:37:20.40	-44:07:31.20	74.3	4.34	-0.78	
S313	00:31:10.76	-44:07:41.70	14.4	1.13	-1.01	
S325	00:34:52.73	-44:07:26.30	10.8	1.31	-1.13	
S347	00:35:38.62	-44:06:03.60	15.9	15.98	-0.20	
S355	00:30:19.00	-44:04:33.40	14.9	5.67	-0.70	
S360	00:34:58.74	-44:04:59.30	26.2	1.95	-0.53	
S371	00:38:54.63	-44:03:29.20	12.1	0.99	-0.37	
S381	00:39:40.19	-44:02:10.20	23.1	2.20	0.19	
S390.1	00:37:19.70	-44:01:49.80	11.0	3.64	-3.13	blends with 390

Table 6: A section of the table with SUMSS counterparts to 1.4 GHz radio sources. Table 6 is published in its entirety in the electronic edition of the *Astronomical Journal*. A portion is shown here for guidance regarding its form and content. *Column 1*: The source names we use in this paper; *Columns 2/3*: SUMMS right ascension and declination; *Column 4*: SUMMS flux density in mJy; *Column 5*: separation of the SUMMS source to the source coordinates in Table 5; *Column 6*: the spectral index; *Column 7*: comment